


Nonlinear ion-stopping calculations for a classical free-electron gas at high projectile energies

R. C. Fadanelli * and P. L. Grande 

*Ion Implantation Laboratory, Instituto de Física, Universidade Federal do Rio Grande do Sul (UFRGS),
Av. Bento Gonçalves 9500, 91501-970, Porto Alegre, Rio Grande do Sul, Brazil*

 (Received 28 November 2022; accepted 6 April 2023; published 19 April 2023)

In this work, we solved the classical equations of motion and Poisson equation self-consistently, equivalent to the nonlinear *Vlasov-Poisson equation*, for a projectile moving in a static free-electron gas to calculate the full noncentral self-consistent electron-ion potential, and thus the ion stopping power. We investigated the origin of the Barkas effect, namely, the first nonlinear effect for projectiles at high velocities responsible for the difference between the energy-loss results for positively and negatively charged ions traversing the same target. This effect is strongly enhanced by the multipolar part of the electron-ion potential as first suggested by Lindhard [J. Lindhard, *Nucl. Instr. and Meth.* **132**, 1438 (1976)]. Moreover, this effect is partially related to the nonconservation of the angular momentum in electron-ion collisions. These nonlinear calculations are applied to understanding the stopping of protons and antiprotons in Al at high projectile energies.

DOI: [10.1103/PhysRevA.107.042812](https://doi.org/10.1103/PhysRevA.107.042812)

I. INTRODUCTION

The stopping power, also called the stopping force, of ions slowing down into the matter is a basic quantity used in many areas of knowledge and different approaches to calculate it are found in the extensive literature [1]. Among them, the free-electron gas (FEG) model has been used to evaluate the electronic stopping because of its simplicity and reliability [2]. It can be also used as a starting point and a reference for more advanced calculations such as time-dependent density functional theory (TDDFT) [3] to check convergence and predictions. The main physical quantity in the FEG model is the electron-ion interacting potential, which is well known in the framework of dielectric formalism or the linearized Vlasov-Poisson equation for a classical plasma. For nonlinear calculations the self-consistent electron-ion interacting potential is still unknown and therefore central potentials determined from the Friedel sum rule have been used [4,5] to calculate the electronic stopping power and the corresponding the Barkas effect [1,6–8] as a function of the projectile energy.

The Barkas effect [9,10], also called Barkas-Andersen [1], is the first correction of the Bethe formula [11] that depends on the sign of the charge of the projectile. At high projectile energies, positively charged ions have larger stopping than negatively charged ions for the same projectile mass and target. This effect was first explained in terms of electron polarization and calculated by Ashley, Ritchie, and Brandt (ARB) [12] and Jackson and McCarthy [13] for distant collisions using classical and quantum calculations, respectively, for an electron harmonically bound. Some useful formulas for the ARB model can be found in [14] and more recently in [11], but they depended on a cutoff distance a . Lindhard [15] also calculated the Barkas effect using a dimensionless analysis and proposed different mechanisms involving close collisions. Experimental data under channeling conditions demonstrated

the validity of the ARB and Lindhard models for the Barkas effect in Si [16,17].

For a FEG the rigorously second-order perturbation theory was applied by Pitarke *et al.* [18]. Numerous articles on this subject can be found in the literature (see, for example, the references in [1]). Most of the articles are limited to the use of either perturbation theory or central potentials to describe the electron-ion interaction. Except for a few *ab initio* coupled-channel and TDDFT calculations [19–21] and distorted wave methods [22–24], full nonlinear calculations of the Barkas effect in a free electron gas system using noncentral ion-electron potentials and classical mechanics are still missing in the literature. While classical calculations are much less computationally demanding, classical Barkas results compare well with the fully quantum mechanical ones [15,18], so that in some cases we can avoid complex quantum mechanical calculations. Moreover, classical calculations can be augmented with quantum mechanical characteristics. One such approach is to incorporate the inverse Bloch correction at high projectile energies [1,25] or even utilize the Bohm quantum mechanical potential [26,27].

To this end, we perform self-consistent stopping-force (dE/dx) calculations corresponding to the full nonlinear Vlasov-Poisson approach for a projectile with velocity \bar{v} and charges $Z_1 > 0$ and $-Z_1$ traversing a homogeneous electron gas at rest with undisturbed density n by using a multipolar expansion for the induced potential. The results for the *Barkas factor*, namely,

$$B = \frac{\frac{dE}{dx}(Z_1) - \frac{dE}{dx}(-Z_1)}{\frac{dE}{dx}(Z_1) + \frac{dE}{dx}(-Z_1)}, \quad (1)$$

were compared to results obtained by Lindhard [15] and ARB [12] with $a = 1/(1.78v)$ [15,28]. It is pointed out that the use of a as the radius of a quantum oscillator will reduce B by a factor of 2 [15]. Furthermore, we calculated the full numerical solution of a projectile with charge $\pm Z_1$ interacting with a classical harmonic oscillator [29], as described in

*raul@if.ufrgs.br

Appendix A, using the PYTHON code described in the Supplemental Material [30]. In addition, the present results were used to calculate the total stopping force of protons and antiprotons in an Al target by assuming a collection of FEGs to represent the Al subshells. Atomic units ($\hbar = m_e = e = 1$) are used in this work unless otherwise stated.

II. THEORETICAL PROCEDURES

In this work, we consider the reference frame where the projectile is at rest, in which the electrons move initially with a velocity $-\vec{v}$ related to the projectile. The initial undisturbed electron density n is given as a function of the Wigner-Seitz radius r_s as $n = \frac{3}{4\pi} r_s^{-3}$. We consider $\vec{r}_{cl}(t, \vec{b})$ as the classical trajectory of each electron at time t and with impact parameter \vec{b} , $V(\vec{r})$ as the total projectile-electron potential energy (including screening), $V_{ind}(\vec{r})$ as the induced potential energy, $V_{bare}(\vec{r})$ as the bare ion-electron potential energy, $\rho(\vec{r})$ as the density in the disturbed electron gas, and $n_{ind}(\vec{r})$ as the induced electron gas density. These quantities are related according to $n_{ind}(\vec{r}) = \rho(\vec{r}) - n$ and $V(\vec{r}) = V_{ind}(\vec{r}) + V_{bare}(\vec{r})$.

We performed self-consistent evaluations of the stopping force, by solving the following coupled equations iteratively:

$$\frac{d^2}{dt^2} \vec{r}_{cl}(t, \vec{b}) = -\nabla V(\vec{r}_{cl}), \quad (2)$$

$$\rho(\vec{r}) = nv \int dt \int d^2b \delta^{(3)}[\vec{r} - \vec{r}_{cl}(t, \vec{b})], \quad (3)$$

$$\nabla^2 V_{ind}(\vec{r}) = -4\pi n_{ind}(\vec{r}), \quad (4)$$

$$c_\ell(r) = 2\pi nv \int_0^\infty db b \int_{-\infty}^\infty dt \Theta(R_{\max} - r_{cl}(t, \vec{b})) P_\ell(\cos \theta_{cl}(t, \vec{b})) \times \left\{ \Theta(r - r_{cl}(t, \vec{b})) \frac{r_{cl}^\ell}{r^{\ell+1}} + \Theta(r_{cl}(t, \vec{b}) - r) \frac{r^\ell}{r_{cl}^{\ell+1}} - \frac{r^\ell r_{cl}^\ell}{R_{\max}^{2\ell+1}} \right\} - \frac{2\pi n}{3} (R_{\max}^2 - r^2) \delta_{0,\ell}, \quad (6)$$

where R_{\max} is a maximum distance in the calculations, $r_{cl}(t, \vec{b}) = |\vec{r}_{cl}(t, \vec{b})|$ is the distance between the electron and the ion, $\theta_{cl}(t, \vec{b})$ is the angle between $\vec{r}_{cl}(t, \vec{b})$ and the z axis, and $\Theta(x)$ is the Heavyside step function.

To achieve convergence, all radial coefficients $c_\ell(r)$ were subject to the condition $c_\ell(r \geq R_{\max}) = 0$, where R_{\max} was chosen typically as $4/\alpha$, corresponding to four times the screening length. Equation (6) was obtained by considering the potentials given by a Green's function for a FEG inside a grounded spherical shell of radius R_{\max} , that is, $V(R_{\max} = 0)$, as described in Appendix B. Using the aforementioned Green's function, $V_{bare}(\vec{r})$, the central Coulomb potential, is given by

$$V_{bare}(\vec{r}) = -Z_1 \left(\frac{1}{r} - \frac{1}{R_{\max}} \right). \quad (7)$$

For practical reasons, the sum in Eq. (5) is truncated to a maximum value of ℓ , denoted as ℓ_{\max} . After describing an adequate

namely, Newton's and Poisson's equations, which are equivalent to the so-called *Vlasov-Poisson* equation [14,31] largely used in plasma physics. The physical interpretation of Eq. (3), described in [25], corresponds to the electron counting in a given volume dV under stationary conditions, by integrating all trajectories of a large electron ensemble, with different impact parameters \vec{b} related to the ion. It was shown that the electron density obtained from Eq. (3) satisfies the Friedel sum rule for central potentials [25]. Given the total potential energy $V(\vec{r})$, each classical trajectory $\vec{r}_{cl}(t, \vec{b})$ is obtained by integrating Eq. (2) numerically via the Verlet algorithm. Each trajectory begins with impact parameter \vec{b} , chosen from an evenly spaced grid. After obtaining the classical trajectories for several electrons, a new interacting potential is evaluated via Eqs. (3) and (4), and the process is repeated until convergence is achieved. For this sake, the new potential should be mixed with typically 95% of the previous one otherwise convergence is not achieved. The initial potential is assumed to have Yukawa-type screening, with inverse screening length given by $\alpha = \omega_p/v$, where $\omega_p = \sqrt{4\pi n}$ [1] is the plasmon frequency. Then, unless defined otherwise, the initial potential energy is a central one. To allow for multipolar effects on both the induced density and the energy loss, the potential energy is, following our system symmetry, expanded via Legendre polynomials [32] as

$$V_{ind}(\vec{r}) = \sum_{\ell=0}^{\infty} c_\ell(r) P_\ell(\cos \theta), \quad (5)$$

where r is the distance between the electron and the projectile and θ is the angle between the direction parallel to the initial electron velocity and the electron position. The radial coefficients $c_\ell(r)$ are given by

number of electron trajectories via $\vec{r}_{cl}(t, \vec{b})$, the energy-loss can be evaluated either from the dipolar part of the induced potential as $c_1(r)/r$ at $r \rightarrow 0$ or by using the following expression [25]:

$$\frac{dE}{dx} = Z_1 nv \int dt \int d^2b \frac{\cos \theta_{cl}(t, \vec{b})}{r_{cl}^2(t, \vec{b})}. \quad (8)$$

In this work, both methods yield the same results within the numerical uncertainties.

The described procedure is performed for projectiles with charge $Z_1 > 0$ and for antiprojectiles with charge $-Z_1$. Finally, the so-called *Barkas factor* from Eq. (1) is evaluated.

III. RESULTS AND DISCUSSION

The above procedure is used for a target modeled by a FEG with $r_s = 2.07$, which realizes the Al valence electrons. The used projectiles were protons and antiprotons

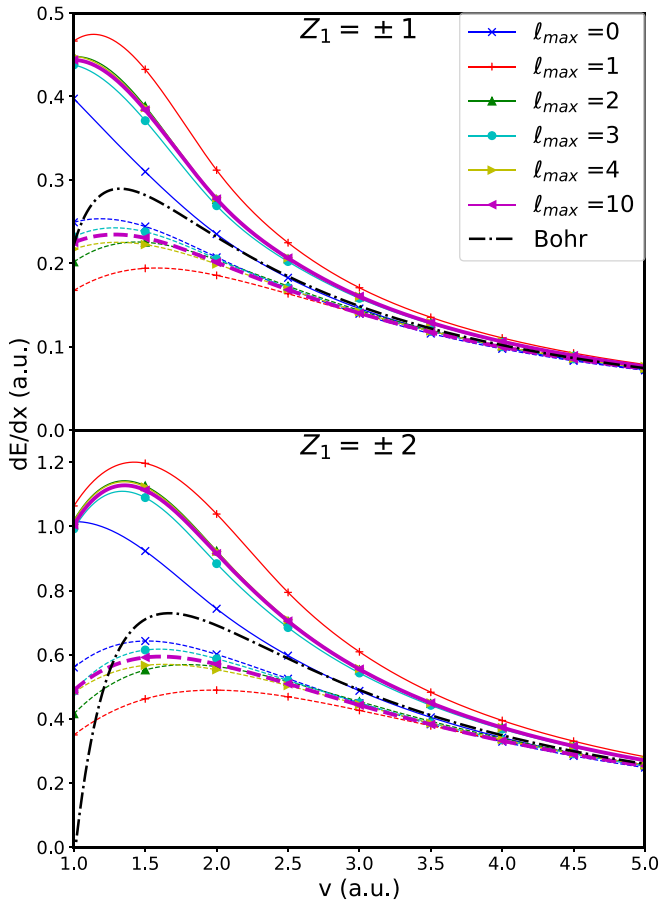


FIG. 1. Self-consistent results of dE/dx for ions (continuous lines) and anti-ions (dashed lines) in Al FEG ($r_s = 2.07$) as a function of the projectile velocity for different values of ℓ_{\max} (indicated by colors) and for $Z_1 = \pm 1$ (top panel) and $Z_1 = \pm 2$ (bottom panel). As a comparison, Bohr stopping results are shown (black dashed-dotted line). The difference in the energy loss for ions and anti-ions for noncentral potentials is larger than the one found by using a central potential ($\ell_{\max} = 0$).

($Z_1 = \pm 1$), helium and antihelium ($Z_1 = \pm 2$), and, to compare the energy-loss results to the ones obtained via perturbation theory, projectiles with $Z_1 = \pm 0.1$ were used.

Figure 1 shows the present calculations for the stopping force as a function of the projectile velocity and different values of the cutoff ℓ_{\max} for the multipolar expansion in Eq. (5). The calculations are compared to the classical Bohr stopping formula [33] recently rederived for a FEG in [25] with the oscillator frequency ω_0 matching the plasmon one ω_p (see black dashed-dotted lines). All calculations converge to the results of the Bohr formula at high projectile velocities. Calculations restricted to a central potential ($\ell_{\max} = 0$) approach faster to the Bohr results whereas calculations with noncentral potentials ($\ell_{\max} > 0$) overestimate (underestimate) the Bohr results for $Z_1 > 0$ ($Z_1 < 0$) for $v > 2$ due to the Barkas effect. The dipolar self-consistent potential ($\ell_{\max} = 1$) overestimates the Barkas effect, but the calculations shows a fast convergence for $\ell_{\max} \geq 4$.

By considering the difference between the stopping forces of the proton and antiproton (top panel), our results show

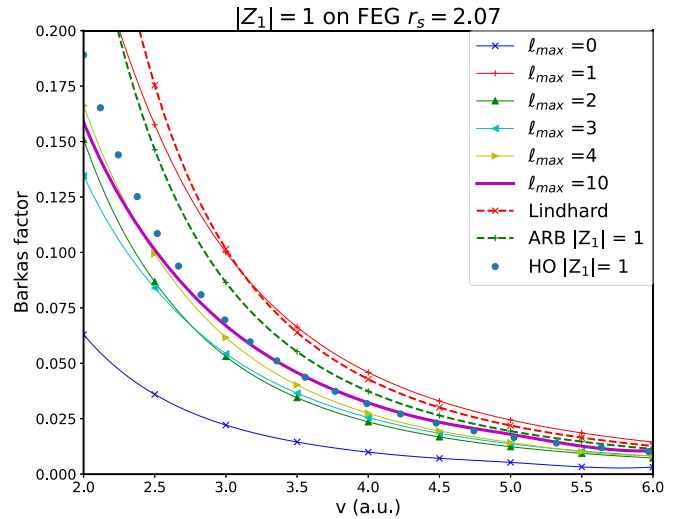


FIG. 2. Self-consistent results of the Barkas factor for $|Z_1| = 1$ (continuous lines), Lindhard [15] and Ashley *et al.* [12] (dashed lines) and classical harmonic oscillator (HO, circles) in Al FEG. For large values of ℓ_{\max} , the self-consistent results approach the results from Lindhard and Ashley and the classical HO results.

that the Barkas factor is strongly increased for noncentral potentials, especially for lower projectile velocities. For heavier ions, the same behavior regarding the Barkas factor can be seen, just enhanced, as shown in the bottom panel. In Fig. 2, our results of the Barkas factor B [see Eq. (1)] for $|Z_1| = 1$ are shown for different values of ℓ_{\max} and compared to the results from Lindhard, ARB, and the classical harmonic oscillator (HO) (using $\omega_0 = \omega_p$) models. For velocities above 3.0 a.u., we find a good agreement between the self-consistent ($\ell_{\max} = 10$) and HO results. The Lindhard results are larger than the ARB ones, but both converge to HO results at high velocities. It is important to point out that ARB and HO, in general, yield different results. This is because ARB evaluations converge to HO only for distant collisions, i.e., those larger than a certain cutoff parameter. On the other hand, HO calculations do not require the use of a cutoff parameter. The calculated Barkas factors using only central potentials ($\ell_{\max} = 0$), however, are noticeably smaller than all presented results particularly the ones using noncentral potentials. This indicates that the Barkas effects depend on the noncentrality of the screening potentials and cannot be described adequately by using only central screening potentials.

Since the agreement among different models for the Barkas factor seems to become better for larger velocities, we investigate the same effects for fictitious projectiles that bear $|Z_1| = 0.1$ to approximate the perturbative conditions (in atomic units, $2Z_1/v \ll 1$) for ion-FEG interaction even for lower ion velocities. The present self-consistent results are shown in Fig. 3 for central potentials ($\ell_{\max} = 0$) and non-central potentials with $\ell_{\max} = 10$, together with the Lindhard, ARB, and HO models. Under perturbative conditions as realized by such fictitious projectiles, the following results are even more evident. HO and $\ell_{\max} = 10$ results have a very good agreement, lying between ARB and 2/3 of the Lindhard results and converging to the ARB and Lindhard results at high velocities. According to Lindhard [15] 2/3 of his suggested

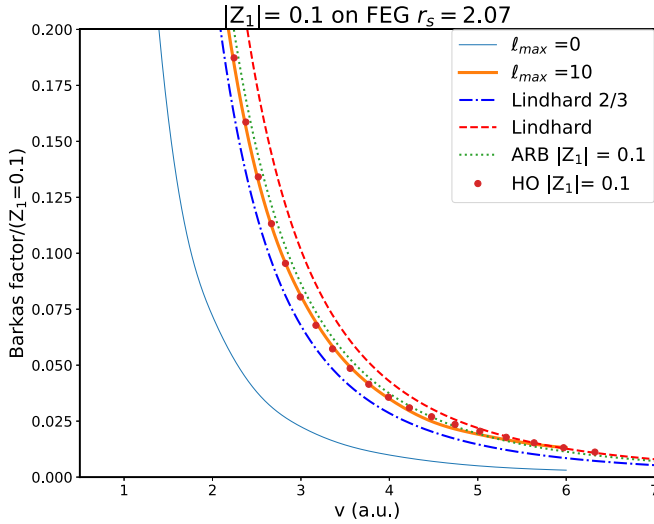


FIG. 3. The same as in Fig. 2 but for fictitious projectiles with $|Z_1| = 0.1$. Note that the present noncentral calculations for $\ell = 0$ converge to the ARB or Lindhard results for large velocities.

Barkas factor comes from projectile screening and $1/3$ from nonconservation of the angular momentum. A Barkas factor amounting values close to $2/3$ of the Lindhard results was also obtained by classical calculations [8] using central potentials, where the angular momentum is conserved, differently from the present work.

The equivalence between the oscillator and FEG models for $\omega_0 = \omega_p$ is well known in first-order perturbation theory [1]. However, this equivalence goes further including the leading term of the Barkas effect as long as the self-consistent noncentral potential is used for FEG calculations. Similar results were reported by Miraglia and Gravielle [24] by using a distorted-wave-like dielectric function called Coulomb-Lindhard [23].

From Figs. 2 and 3 we can also observe that no other model agrees with the self-consistent results for central potentials, further indicating that the Barkas effect is strongly enhanced by noncentral potentials. Indeed our calculations show a strong increase of the induced potential $V_{\text{ind}}(\vec{r})$ at $r = 0$ when at least the dipole part of the potential is added. According to the Lindhard model [15], this extra screening will reduce (increase) the local velocity at the distance of the closest approach increasing (decreasing) the scattering intensity for positively (negatively) charged ions. Figure 4 shows the induced potential calculated at the position of the projectile ($r = 0$) of a fictitious charge $Z_1 = 0.1$ as a function of the projectile velocity. For calculations restricted to a central potential ($l_{\text{max}} = 0$) the induced potential at $r = 0$ agrees with the one obtained from the Friedel sum rule [4] at high projectile velocities for a Yukawa potential with inverse of screening length $\alpha = \omega_p/v$. For a noncentral electron-ion potential the induced potential at $r = 0$ or equivalently the screening around the projectile increases in accordance with the value predicted by the dielectric formalism at high projectile velocities, namely, $\alpha = 0.5\pi \omega_p/v$ [34]. By allowing for further terms in the multipole expansion in Eq. (5) the monopole contribution decreases (being more screened) to

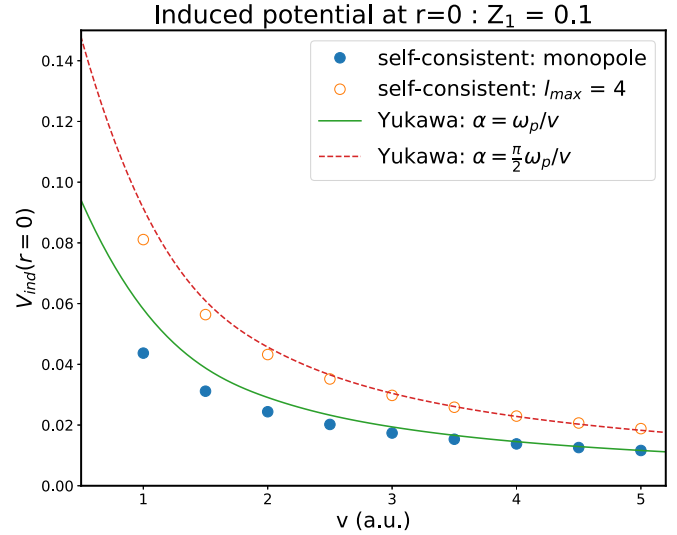


FIG. 4. Self-consistent results for the induced potential at the ion position as a function of the ion velocity with charge $Z_1 = 0.1$ for a FEG with $r_s = 2.07$ a.u. The lines correspond to the induced potential at $r = 0$ from a Yukawa potential with inverse of screening length given by α .

compensate for the extra scattering from the $\ell > 0$ terms in a self-consistent calculation. As discussed in [15], the screening effect around the projectile is directly responsible for the Barkas effect and therefore it will be enhanced in comparison to the one obtained by restricting the electron-ion potential to a single monopole (central) contribution.

Moreover, by using only central potentials to describe the changes in n , there is, as expected, no change between the initial and final electron angular momentum related to the ion for all initial momentum values. However, by using noncentral potentials, the ion-perturbed FEG combination behaves also as a dipole because of the accumulation (or depletion) of the electron behind the ion, leading to the nonconservation of the angular momentum, as shown in Fig. 5. Indeed, for large angular momenta, we can see that the electron angular momentum is increased for positive ions and decreased for negative ones compared to the case of a central potential. Also, as displayed in Fig. 5, the change is not symmetric between both positive and negative projectiles. However, they become more symmetrical in the perturbative regime as shown in Fig. 6 for fictitious $Z_1 = \pm 0.1$ ions. A slight increase (decrease) of angular momentum relative to the initial one will cause a slight increase (decrease) of the angle between the electron position and linear momentum. As observed in the calculated electron trajectories for positively (negatively) charged ions this change will slightly decrease (increase) the angular position θ_{cl} and therefore according to Eq. (8) will slightly increase (decrease) the stopping force for positively (negatively) charged projectiles. This explains the extra mechanism for the Barkas effect in the perturbative regime proposed by Lindhard [15], which amounts to $1/3$ of the value given by Lindhard. However, for smaller electron angular momenta (either small impact parameters or smaller velocities or a combination of both), there are a few differences in the electron angular momentum change for ions or anti-ions as

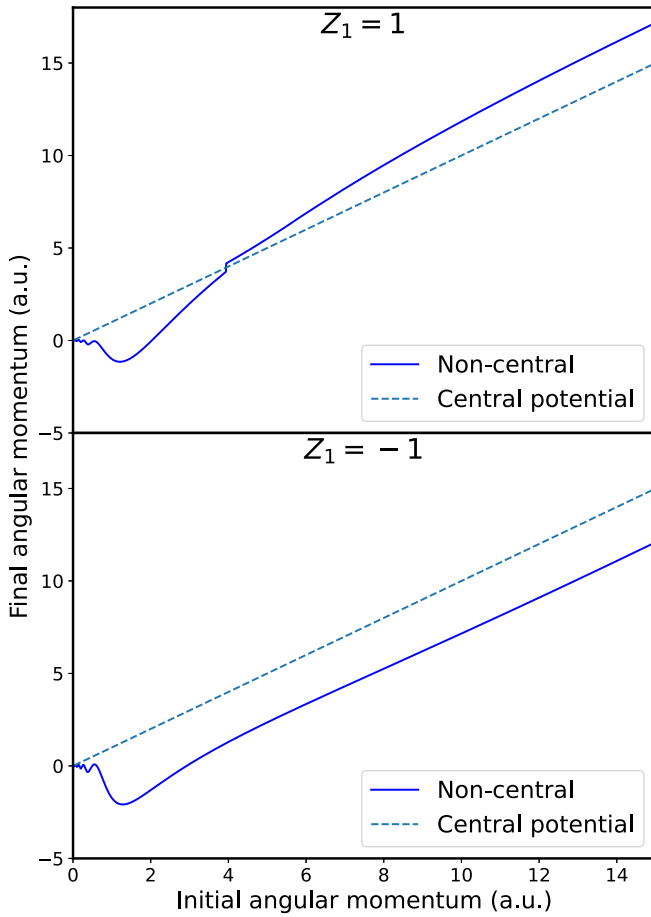


FIG. 5. Final versus initial angular momentum for scattered electrons by protons (top panel) and by antiprotons (bottom panel) for $v = 5$ a.u. and $r_s = 2.07$ and self-consistent $\ell_{\max} = 0$ (dashed lines) and $\ell_{\max} = 10$ (continuous lines) potentials. As expected, a central potential ($\ell_{\max} = 0$) does not change the electron angular momentum, while noncentral potential can even invert the sign of the angular momentum, see text.

observed in Fig. 5. Even an inversion of the electron angular momentum is observed at 2 a.u. and 3 a.u. for protons and antiprotons, respectively. Nevertheless, the region of angular momenta where this takes place vanishes in the perturbative limit as shown in Fig. 6 for fictitious $Z_1 = \pm 0.1$ ions.

Finally, in Fig. 7 we provide a comparison with experimental data for proton and antiprotons in Al. For this sake, we used a collection of FEGs according to ICRU recommendations [1]. Namely, we used two FEGs with $r_s = 0.46$ and $r_s = 2.07$ realizing the L ($2p$) and M shells of Al, respectively. The K and L ($2s$) shells were not included in what follows because they are of minor importance for the present projectile velocity range $v < 6$ a.u. According to the Bohr's criterion [1,35] for the validity of the classical calculations $\kappa = 2Z_1/v$ should be larger than 1. Since, for the present case κ ranges from $1/3$ to $2/3$, we added the inverse Bloch correction as demonstrated in [25] and used in stopping power programs as, e.g., PASS [36] to add quantum mechanical features to our classical calculations. It should be pointed out, however, that the inverse Bloch correction can be used only at high velocities and relates only to scattering in the Coulomb

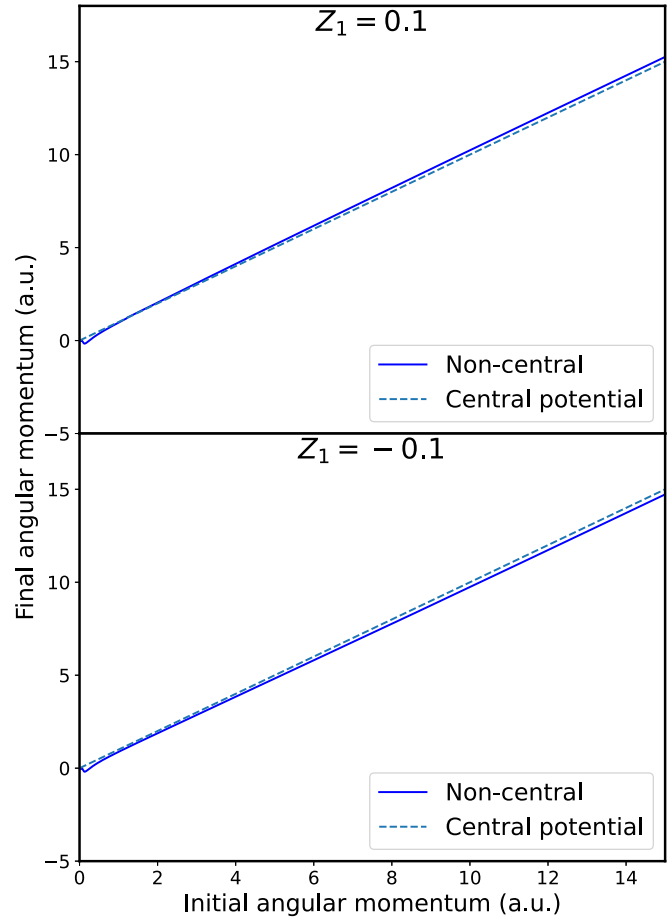


FIG. 6. The same as in Fig. 5 for $Z_1 = \pm 0.1$. Differently from Fig. 5, it is possible to see symmetry in the angular momentum change for scattered electrons by ions and anti-ions for larger momentum values.

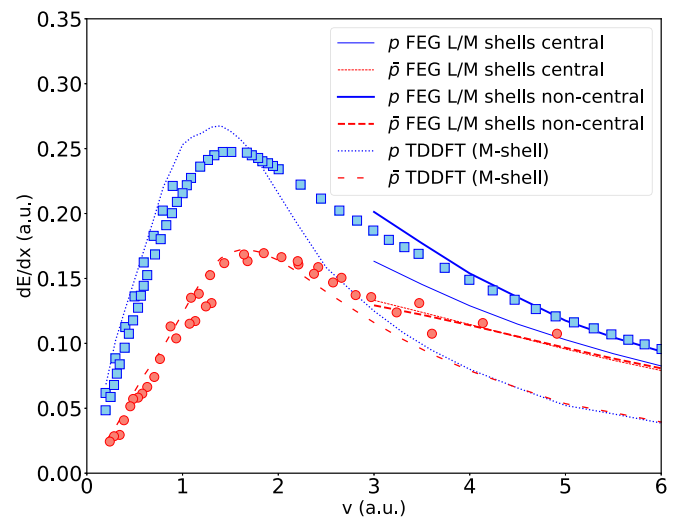


FIG. 7. Experimental (symbols: squares for protons and circles for antiproton) [37,38] and theoretical (lines, see legend) results for the stopping of protons (p) and antiprotons (\bar{p}) in Al as a function of the ion velocity. The lines stand for our self-consistent calculations (FEG) and the TDDFT evaluations [20].

potential. There is no corresponding quick-fix for quantum mechanical effects or corrections to the electron density induced according to classical mechanics. The results were then averaged according to the velocity distribution of a degenerated electron gas allowing a better description for the shell corrections [1] of the Al $L(2p)$ shell.

Overall, a good agreement between the self-consistent and experimental results is obtained for velocities above 3 a.u. as can be seen in Fig. 7. Because the present calculations assume a FEG at rest we did not present any evaluations for $v < 3$ a.u. Since we consider a frozen classical FEG, our model does not describe all possible incoming directions and velocities for the scattered electrons. These effects become increasingly considerable at smaller projectile velocities. The experimental results for proton and antiproton energy losses in Al as a function of the ion velocity are given in [37] and [38]. The self-consistent results for $\ell_{\max} = 0$ and $\ell_{\max} = 10$ are shown for protons and antiprotons. Especially for protons, the use of noncentral potentials is necessary for a better agreement between experimental and theoretical results. For swift antiprotons, however, noncentral components for the potential seem to play a minor role in the energy-loss results. In fact, according to Fig. 1 the self-consistent calculations for $\ell_{\max} = 0$ and $\ell_{\max} = 10$ are more different for protons than for antiprotons. Therefore, for the energy range where the experimental data are available the Barkas effect cannot be treated as perturbative, where the effect must be symmetrical for both projectiles. For smaller projectile energies, TDDFT results for interaction between protons or antiprotons and valence (M shell) Al electrons [20] are given for comparison, depicting considerable Barkas effect for smaller energies.

IV. CONCLUSION

We provided stopping-force and Barkas-factor results for bare ions traversing a classical frozen (at rest) free electron gas, evaluated by the nonlinear Vlasov-Poisson equations for central and noncentral screening potentials for the ion. The results indicated that classical FEG evaluations using only central potentials are not enough to describe the Barkas effect of the stopping, especially for fast projectiles. However, for slower projectiles in a more realistic (nonstatic) FEG, noncentral effects on the potential are expected to vanish.

The present calculations agree with ARB and Lindhard-Barkas results only at very high projectile energies where the Barkas effect is indeed very small. For the energy range where the Barkas effect is of some importance (at lower velocities), the present calculations better agree with $2/3$ of the Lindhard values. This is because changes in the angular momentum are only symmetrical and effective in the perturbative limit. This can explain the fact that the Barkas effect should be reduced from ARB values as demonstrated recently by Salvat [11] who analyzed the stopping data at high energies using the Bethe formula and its corrections.

Even for protons the perturbative approach to obtain the Barkas effect at few hundred of keV/u is not suitable since noncentral potential effects are more important for protons than for antiprotons. Finally, the present stopping calculations agree with the experimental data of protons and antiprotons in Al at high projectile energies showing the importance of the

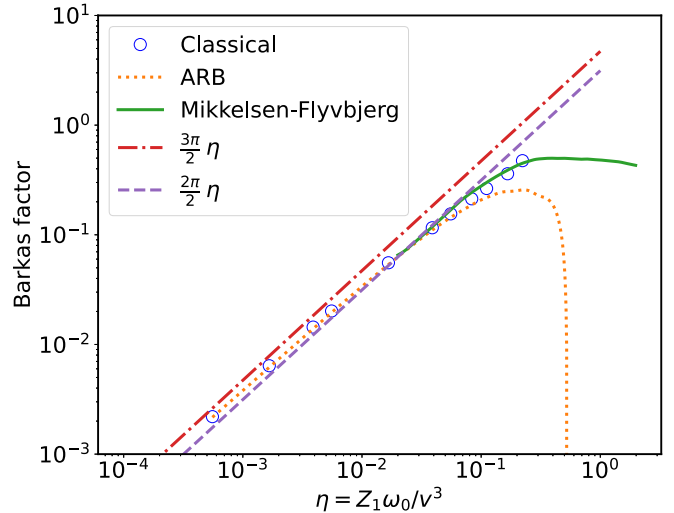


FIG. 8. Calculations of the Barkas factor Eq. (1) as a function of the dimensionless parameter $\eta = Z_1\omega_0/v^3$. Open circles correspond to solutions of the classical equations for an electron harmonically bound according to provided PYTHON algorithm. The lines are the results of quantum (green line) [39] and ARB calculations for $b_{\min} = 2Z_1/v^2$ (orange line) [11]. Dashed lines show different trends of the Barkas factor (see text).

Barkas effect and its asymmetry for protons and antiprotons at the high-energy range of the available experimental data.

This work suggests the use of the Bohmian mechanics to convert the present classical calculations into fully quantum mechanical ones [26,27] by utilizing the Bohm quantum mechanical potential which is based on the electronic density and evaluated from the trajectories as in Eq. (3). This approach can offer an alternative to the traditional quantum calculations for the electronic stopping power.

ACKNOWLEDGMENTS

This study was financed, in part, by the Coordenação de Aperfeiçoamento de Pessoal de Nível Superior, Brazil (CAPES), Finance Code 001, by FINEP, by the Conselho Nacional de Desenvolvimento Científico e Tecnológico (CNPq), by the Instituto Nacional de Engenharia de Superfícies (INES) and PRONEX-FAPERGS. The authors also thank Y. Levin and R. Pakter for enlightening discussions.

APPENDIX A: CLASSICAL HARMONIC OSCILLATOR

The stopping cross section for a classical collision between a projectile with charge Z_1 and velocity v and an electron harmonically bound with frequency ω_0 is calculated using quantum [39] and classical [29] mechanics. In this work we obtain the classical solution of this problem by solving directly the corresponding Newton's equations through the ODEINT function from the SCIPY PYTHON package [40]. A simple code is available in the Supplemental Material [30].

Figure 8 shows the Barkas factor Eq. (1) as a function of the dimensionless parameter $\eta = Z_1\omega_0/v^3$. Classical calculations (open circles) agree with ARB [12] calculations for $\eta \ll 1$ as expected from the ARB model. Quantum calculations

performed by Mikkelsen and Flyvberg agree with the classical ones. This shows that quantum effects are of less importance for the Barkas effect in the harmonic oscillator target. The dashed lines show two predictions of the Lindhard model [15] for the Barkas effect. One of them corresponds to 2/3 of the original one where only screening effects at $r = 0$ are considered. Although it does not correspond to the exact asymptotic solution at $\eta \rightarrow 0$, it provides a better agreement with classical and quantum calculations for the cases where the Barkas effect is not too small.

APPENDIX B: EXPANDING THE INDUCED POTENTIAL IN SPHERICAL HARMONICS

To achieve convergence for the classical equations, we consider the electrostatic potential for an arbitrary charge distribution *inside* a grounded conductive sphere of radius R_{\max} . Therefore, all evaluated potentials are subject to the boundary condition $V(r \geq R_{\max}, \theta, \phi) = 0$.

In this work, we use an approach described in [41], in which the Green's function inside the conductive sphere is obtained by solving

$$\nabla^2 G(\vec{r}, \vec{r}') = -4\pi \delta(\vec{r} - \vec{r}'), \quad (\text{B1})$$

using the aforementioned boundary conditions (the so-called Dirichlet conditions). In Eq. (B1), \vec{r} is the point where we evaluate the potential and \vec{r}' is the integration variable to determine the aforementioned potential. The prime in the Laplacian operator indicates that the derivatives should be taken related to \vec{r}' .

The solution of Eq. (B1) can be shown as

$$G(\vec{r}, \vec{r}') = \frac{1}{|\vec{r} - \vec{r}'|} - \frac{R_{\max}}{r' |\vec{r} - \frac{R_{\max}^2}{r'^2} \vec{r}'|}. \quad (\text{B2})$$

Equation (B2) can be rewritten in spherical coordinates as

$$G(\vec{r}, \vec{r}') = \frac{1}{\sqrt{r^2 + r'^2 - 2rr' \cos \alpha}} - \frac{1}{\sqrt{\frac{r^2 r'^2}{R_{\max}^2} + R_{\max}^2 - 2rr' \cos \alpha}}, \quad (\text{B3})$$

where α is the angle between \vec{r} and \vec{r}' . It is possible, in a procedure analogous to the one used in [41], to expand $G(\vec{r}, \vec{r}')$ inside the sphere as

$$G(\vec{r}, \vec{r}') = 4\pi \sum_{\ell=0}^{\infty} \frac{1}{2\ell+1} \sum_{m=-\ell}^{\ell} \left(\frac{r_{<}^{\ell}}{r_{>}^{\ell+1}} - \frac{r^{\ell} r'^{\ell}}{R_{\max}^{2\ell+1}} \right) \times Y_{\ell}^m(\theta, \phi) Y_{\ell}^{m*}(\theta', \phi'), \quad (\text{B4})$$

where $r_{<} = \min\{r, r'\}$, $r_{>} = \max\{r, r'\}$, and $Y_{\ell}^m(\theta, \phi)$ are the spherical harmonics as functions of the polar angle θ and the azimuthal angle ϕ [41].

Finally, as $V(r = R_{\max}, \theta, \phi) = 0$, we have

$$V_{\text{ind}}(\vec{r}) = \int_{r' \leq R_{\max}} [\rho(\vec{r}') - n] G(\vec{r} - \vec{r}') d^3 r', \quad (\text{B5})$$

where ρ is the charge density. Finally, by inserting Eq. (B4) in Eq. (B5), using Eq. (3), and using the azimuthal symmetry of the system ion-FEG, as well as the addition theorem for spherical harmonics [41], we obtain Eq. (6).

-
- [1] P. Sigmund, *Particle Penetration and Radiation Effects*, 1st ed., Vol. 1 (Springer-Verlag, Berlin, 2006), p. 151.
- [2] R. H. Ritchie, *Phys. Rev.* **114**, 644 (1959).
- [3] A. A. Correa, *Comput. Mater. Sci.* **150**, 291 (2018).
- [4] A. F. Lifschitz and N. R. Arista, *Phys. Rev. A* **57**, 200 (1998).
- [5] F. Matias, R. C. Fadaneli, P. L. Grande, N. E. Koval, R. D. Muiño, A. G. Borisov, N. R. Arista, and G. Schiwietz, *J. Phys. B: At., Mol. Opt. Phys.* **50**, 185201 (2017).
- [6] N. R. Arista and A. F. Lifschitz, *Phys. Rev. A* **59**, 2719 (1999).
- [7] C. D. Archubi, I. Abril, R. Garcia-Molina, and N. R. Arista, *Nucl. Instrum. Methods Phys. Res., Sect. B* **316**, 88 (2013).
- [8] N. R. Arista, P. L. Grande, and A. F. Lifschitz, *Phys. Rev. A* **70**, 042902 (2004).
- [9] W. H. Barkas, W. Birnbaum, and F. M. Smith, *Phys. Rev.* **101**, 778 (1956).
- [10] H. Andersen, H. Simonsen, and H. Sørensen, *Nucl. Phys. A* **125**, 171 (1969).
- [11] F. Salvat, *Phys. Rev. A* **106**, 032809 (2022).
- [12] J. C. Ashley, R. H. Ritchie, and W. Brandt, *Phys. Rev. B* **5**, 2393 (1972).
- [13] J. D. Jackson and R. L. McCarthy, *Phys. Rev. B* **6**, 4131 (1972).
- [14] T. Peter and J. Meyer-ter-Vehn, *Phys. Rev. A* **43**, 1998 (1991).
- [15] J. Lindhard, *Nucl. Instrum. Methods* **132**, 1 (1976).
- [16] G. de M. Azevedo, P. L. Grande, M. Behar, J. F. Dias, and G. Schiwietz, *Phys. Rev. Lett.* **86**, 1482 (2001).
- [17] L. L. Araujo, P. L. Grande, M. Behar, J. F. Dias, A. F. Lifschitz, N. R. Arista, and G. Schiwietz, *Phys. Rev. A* **70**, 032903 (2004).
- [18] J. M. Pitarke, R. H. Ritchie, and P. M. Echenique, *Phys. Rev. B* **52**, 13883 (1995).
- [19] A. Salin, A. Arnau, P. M. Echenique, and E. Zaremba, *Phys. Rev. B* **59**, 2537 (1999).
- [20] M. Quijada, A. G. Borisov, I. Nagy, R. Díez Muiño, and P. M. Echenique, *Phys. Rev. A* **75**, 042902 (2007).
- [21] P. Grande and G. Schiwietz, *Nucl. Instrum. Methods Phys. Res., Sect. B* **132**, 264 (1997).
- [22] G. Schiwietz, U. Wille, R. D. Muiño, P. D. Fainstein, and P. L. Grande, *J. Phys. B: At., Mol. Opt. Phys.* **29**, 307 (1996).
- [23] J. E. Miraglia, *Phys. Rev. A* **68**, 022904 (2003).
- [24] J. E. Miraglia and M. S. Gravielle, *Phys. Rev. A* **72**, 042902 (2005).
- [25] P. L. Grande, *Phys. Rev. A* **104**, 012807 (2021).
- [26] D. Bohm, *Phys. Rev.* **85**, 166 (1952).
- [27] F. Haas, *Quantum Plasmas: An Hydrodynamic Approach*, Springer Series on Atomic, Optical, and Plasma Physics (Springer, New York, 2011).
- [28] J. C. Ashley, *J. Phys.: Condens. Matter* **3**, 2741 (1991).
- [29] M. M. Jakas, F. J. Pérez de la Rosa, and E. R. Custidiano, *Phys. Rev. A* **68**, 032903 (2003).
- [30] See Supplemental Material at <http://link.aps.org/supplemental/10.1103/PhysRevA.107.042812> for the PYTHON source code

- used in the evaluation of the ion energy-loss for a harmonically bound electron.
- [31] H. E. J. Koskinen, Vlasov theory, in *Physics of Space Storms: From the Solar Surface to the Earth* (Springer, Berlin, 2011), pp. 141–162.
- [32] M. Abramowitz and I. A. Stegun, *Handbook of Mathematical Functions with Formulas, Graphs, and Mathematical Tables*, Applied Mathematics Series (U.S. Government Printing Office, Washington, D.C., 1972).
- [33] N. Bohr, *London, Edinburgh Dublin Philos. Mag. J. Sci.* **25**, 10 (1913).
- [34] J. Lindhard, K. Dan. Vidensk. Selsk. Mat.-Fys. Medd. **28**, 1 (1954).
- [35] N. Bohr, *The Penetration of Atomic Particles Through Matter*, Kongelige Danske Videnskabernes Selskab. Matematisk-fysiske meddelelser, Vol. 18(8) (1948), p. 1.
- [36] A. Schinner and P. Sigmund, *Nucl. Instrum. Methods Phys. Res., Sect. B* **460**, 19 (2019).
- [37] S. P. Møller, E. Uggerhøj, H. Bluhme, H. Knudsen, U. Mikkelsen, K. Paludan, and E. Morenzoni, *Phys. Rev. A* **56**, 2930 (1997).
- [38] S. P. Møller, A. Csete, T. Ichioka, H. Knudsen, U. I. Uggerhøj, and H. H. Andersen, *Phys. Rev. Lett.* **93**, 042502 (2004).
- [39] H. H. Mikkelsen and H. Flyvbjerg, *Phys. Rev. A* **45**, 3025 (1992).
- [40] P. Virtanen, R. Gommers, T. E. Oliphant, M. Haberland, T. Reddy, D. Cournapeau, E. Burovski, P. Peterson, W. Weckesser, J. Bright, S. J. van der Walt, M. Brett, J. Wilson, K. J. Millman, N. Mayorov, A. R. J. Nelson, E. Jones, R. Kern, E. Larson, C. J. Carey *et al.*, *Nat. Methods* **17**, 261 (2020).
- [41] J. D. Jackson, *Classical Electrodynamics*, 3rd ed. (John Wiley and Sons, Hoboken, NJ, 1998).